ACS APPLIED ENERGY MATERIALS

www.acsaem.org Article

Experimental and Theoretical Study into Interface Structure and Band Alignment of the $Cu_2Zn_{1-x}Cd_xSnS_4$ Heterointerface for Photovoltaic Applications

Sachin R. Rondiya, Yogesh Jadhav, Nelson Y. Dzade, Raihan Ahammed, Tanmay Goswami, Abir De Sarkar, Sandesh Jadkar, Santosh Haram, and Hirendra N. Ghosh*

Cite This: *ACS Appl. Energy Mater.* 2020, 3, 5153−5162 Read Online

ACCESS | Metrics & More | Article Recommendations | Supporting Information

ABSTRACT: To improve the constraints of kesterite Cu_2ZnSnS_4 (CZTS) solar cell, such as undesirable band alignment at p−n interfaces, bandgap tuning, and fast carrier recombination, cadmium (Cd) is introduced into CZTS nanocrystals forming $Cu_2Zn_{1-x}Cd_xSnS_4$ through cost-effective solution-based method without postannealing or sulfurization treatments. A synergetic experimental−theoretical approach was employed to characterize and assess the optoelectronic properties of $Cu_2Zn_{1-x}Cd_xSnS_4$ materials. Tunable direct band gap energy ranging from 1.51 to 1.03 eV with high absorption coefficient was demonstrated for the $Cu_2Zn_{1-x}Cd_xSnS_4$ nanocrystals with changing Zn/Cd ratio. Such bandgap engineering in $Cu_2Zn_{1-x}Cd_xSnS_4$ helps in effective carrier separation at interface. Ultrafast spectroscopy reveals a longer lifetime and efficient separation of photoexcited charge carriers in Cu_2CdSnS_4 (CCTS) nanocrystals compared to that of CZTS. We found that there exists a type-II staggered band alignment at the CZTS (CCTS)/CdS interface, from cyclic voltammetric (CV) measurements, corroborated by first-principles density functional theory (DFT) calculations, predicting smaller conduction band offset (CBO) at the CCTS/CdS interface as compared to the CZTS/CdS interface. These results point toward efficient separation of photoexcited carriers across the p−n junction in the ultrafast time scale and highlight a route to improve device performances.

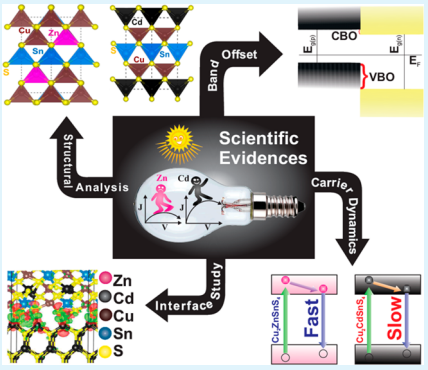

KEYWORDS: *earth-abundant material, cation substitution, interfacial engineering, grain boundary, band offset, ultrafast carrier dynamics, photovoltaic*

INTRODUCTION

The advancement of safe, renewable, and low-cost clean energy technologies to substitute the environmentally unfriendly provider of fossil fuels have attracted significant scientific interest in recent years. Solar cell technology, which harnesses the enormous amount of the Sun's energy to directly produce electricity, is a viable option with obvious socioeconomic and environmental benefits. However, solar devices must be made of inexpensive and earth-abundant materials before photovoltaic (PV) technology can readily provide a significant fraction of the world's energy demands at reduced cost.[1,2] Earth-abundant, nontoxic, and low-cost Cu-based materials Cu_2MSnX_4 (M = Zn, Ni, Fe, Co, Cd and x = S, Se) are attractive potential alternatives to silicon-based PV technology, due to their wide tunable direct bandgap (1.5−1.0 eV) across the visible region, high absorption coefficient ($\sim 10^4$ cm^{-1}), and high carrier mobility (0.1−35 $cm^2V^{-1}s^{-1}$).[3] Besides, the outstanding theoretical efficiency of 31% (according to Schockley Queisser limit) makes Cu_2MSnX_4 materials competitive candidates for environmentally friendly, low-cost, and scalable thin-film PV applications.[4] Cu_2MSnX_4-based materials are also interesting candidates for a wide variety of other applications, including photodetectors,[5] photocatalysis,[6] hydrogen production,[7] photoelectrochemical cell,[8] and batteries.[9]

The first Cu_2ZnSnS_4 (CZTS) solar cell was made-up of vacuum technique and generated a conversion efficiency of 0.66%.[10] So far the kesterite CZTSSe-based PV cells show the highest conversion efficiency of 12.6% as reported by the group of Mitzi.[11] Currently, many research efforts are focused on cation and anion exchange for the enhancement of the conversion efficiencies of CZTS materials. Wong and coworkers have reported conversion efficiencies of 9%[12] for single cation substitution (Cd for Zn) and 10% for double cation substitution (Cd for Zn and Ag for Cu) in CZTS thin

Received: November 27, 2019
Accepted: May 5, 2020
Published: May 5, 2020

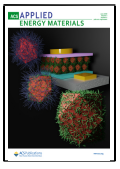

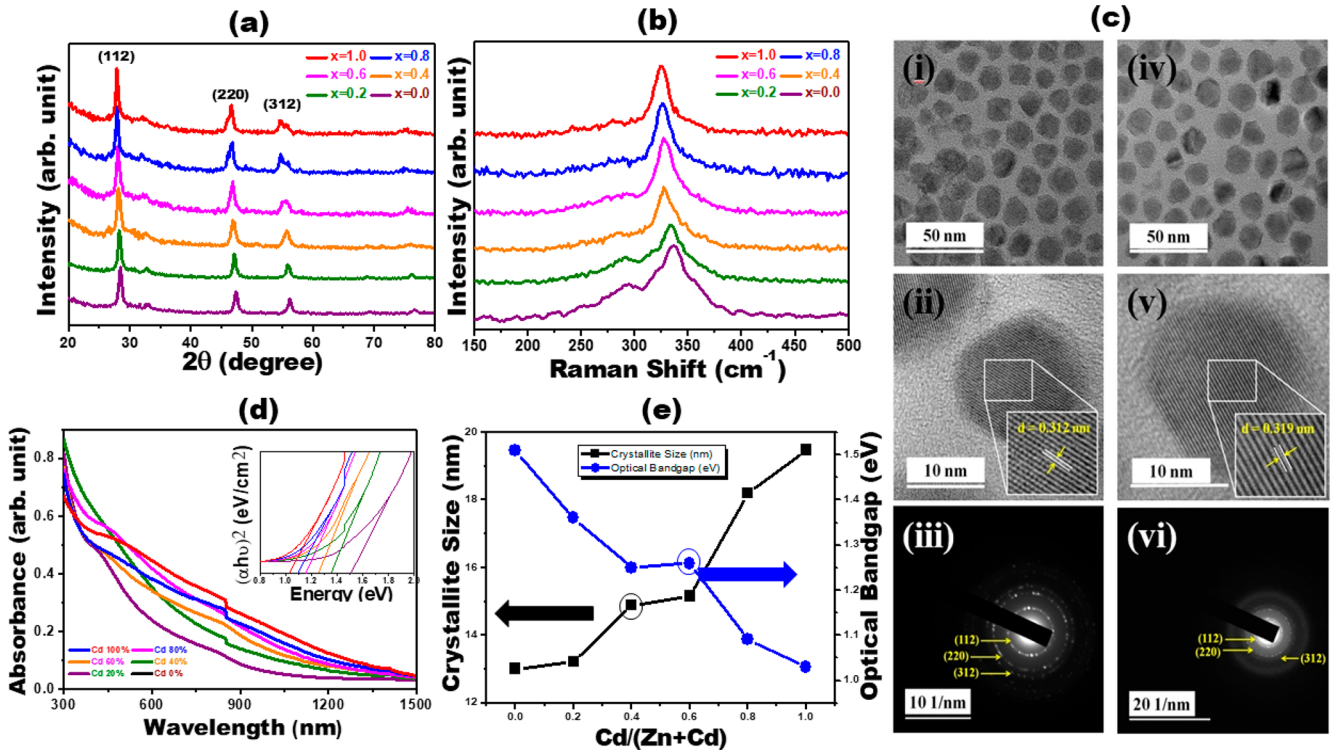

Figure 1. (a) X-ray pattern and (b) Raman spectra (excitation wavelength, 532 nm) for the $Cu_2Zn_{1-x}Cd_xSnS_4$ nanocrystals (x = 0.0−1.0). (c) (i,iv) Low-resolution TEM images recorded for CZTS and CCTS nanocrystals, respectively. (ii,v) HR-TEM image of CZTS and CCTS nanocrystals with clear lattice resolution. An interplanar spacing of 0.312 and 0.319 nm for CZTS and CCTS nanocrystals respectively is clearly visible. (iii,vi) SAED pattern of a single nanocrystal corresponds to the polycrystalline nature of CZTS and CCTS nanocrystals, respectively. (d) The UV−vis-NIR absorbance spectra for $Cu_2Zn_{1-x}Cd_xSnS_4$ nanocrystals with the inset showing the tauc plot. (e) The variation in crystallite size and optical bandgap as a function of cation substitution.

film based solar cells.[13] Despite the recent improvements in Cd-substituted CZTS materials, information regarding the influence of thin film grains, the nature of interfaces between the absorber and buffer layers, and charge carrier dynamics in the Cd-substituted CZTS nanocrystals remained unresolved. The performance of polycrystalline PV cells can be significantly influenced by charge carrier dynamics and grain boundary engineering,[14−17] hence their deep understanding in Cu-based quaternary chalcogenides will assist future optimization of PV devices to achieve improved performance. In earlier investigations,[18−22] we have reported a direct correlation between efficiency and carrier dynamics in solar cells. Solar device performance can be significantly enhanced with elongated charge-carrier lifetimes when the grain size is increased from a few hundred nanometers to the micrometer level.[11] The work of Seto et al. explained how larger grain boundaries can reduce the quantity of defects due to partial atomic bonding.[23] A reduction in the trapping states can thus lead to an increase in the number of free carriers available for electrical conduction. Cation and anion substitution have been employed to tune the bandgap of CZTS materials in progression toward CZTS thin-film solar cells.[12,13,24] Low efficiencies of CZTS-based PV cells have been attributed to several factors including defects, poor interface chemistry, inefficient charge separation due to poor band offsets, and carrier trapping. However, until now there has been no systematic study dedicated to providing detailed insight into the carrier dynamics and interface chemistry in $Cu_2Zn_{1-x}Cd_xSnS_4$ thin films, which makes this investigation timely.

In this communication, we present a synergetic experimental and computational evidence of the beneficial role of cation exchange (Cd for Zn) in $Cu_2Zn_{1-x}Cd_xSnS_4$. High quality and crystalline thin films (RMS roughness below 20 nm) with large grain boundaries were obtained from a unique cost-effective, benchtop solution-processed method, at room temperature without postannealing or sulfurization, which is important in reducing cost of device fabrication. X-ray diffraction and Raman spectroscopy confirmed the nanocrystals without impurity phases. We expect that there is a huge opportunity to improve the device performance with band alignment optimization and monitoring of charge transfer dynamics. Bandgap modulation from 1.51 to 1.03 eV was achieved with growing Cd content in $Cu_2Zn_{1-x}Cd_xSnS_4$ from UV−visible−NIR spectroscopy. The photoexcited charge carrier dynamics, which dictates the photovoltaic performance of $Cu_2Zn_{1-x}Cd_xSnS_4$, was demonstrated with the help of transient absorption spectroscopy where we observed longer charge carrier lifetime in CCTS compared to the CZTS nanocrystals. A type-II band alignment was demonstrated at the CZTS/CdS and CCTS/CdS heterointerfaces through CV measurements and validated by first-principles DFT calculations. Smaller conduction offsets of 0.15 eV (0.11 from DFT) were observed at CCTS/CdS compared to 0.23 eV (0.21 from DFT) at CZTS/CdS interface, suggesting lesser resistance to electron transport across the CCTS/CdS interface. Our results highlight a route to improved solar cell efficiencies through cation substitution and interface band offset optimization.

https://dx.doi.org/10.1021/acsaem.9b02314
ACS Appl. Energy Mater. 2020, 3, 5153−5162

EXPERIMENTAL SECTION

Synthesis. Herein, the colloidal synthesis of $Cu_2Zn_{1-x}Cd_xSnS_4$ (x = 0 corresponds to CZTS and x = 1 corresponds to CCTS) nanocrystals was carried out as per our previous report using a homemade hot injection setup.[25] In a typical synthesis of CZTS nanocrystals, all three metal (copper, zinc, and tin) acetylacetonate precursors with 2:1:1 ratio are dissolved in 15 mL of oleylamine under high purity nitrogen in a three neck flask. The CCTS nanocrystals were similarly synthesized as mentioned above where instead of zinc, cadmium acetate is used in a separate three neck flask. The solutions for both CZTS and CCTS were heated under nitrogen with constant stirring and degassed for 1 h at ∼135 °C. The temperature was set at 240 °C for the injection of sulfur precursor. Fresh 3 mL of sulfur-oleylamine (1 M) solution was injected in the three neck flask and maintained at 260 °C for 1 h for nanocrystal growth. The reaction was quenched by injecting toluene and propanol mixture (1:8), followed by purification of the nanocrystals from unreacted precursors by centrifugation.[25] The intermediate compositions of $Cu_2Zn_{1-x}Cd_xSnS_4$ nanocrystals with x = 0.2, 0.4, 0.6, and 0.8 mmol of Zn/Cd were carried out by similar method discussed in earlier section.

Characterization. Different properties of $Cu_2Zn_{1-x}Cd_xSnS_4$ were characterized using various experimental techniques. X-ray diffraction (XRD) spectra were recorded by X-ray diffractometer (Bruker D8 Advance, Germany). The phase characterization of the as-synthesized samples was obtained by Raman spectroscopy with "Renishaw Raman Microscope" using a wavelength of 532 nm of Nd:YAG laser, in the backscattering geometry. High-resolution transmission electron microscopy (HR-TEM) (TECNAI G2-20-TWIN) was used to obtain high-resolution micrographs and selected area electron diffraction (SAED) patterns. Atomic force microscopy (NC-AFM; JEOL, JSPM-5200) provided micrographs for the investigation of the surface topology in noncontact mode. The compositional details of $Cu_2Zn_{1-x}Cd_xSnS_4$ nanocrystals were obtained from energy dispersive X-ray spectroscopy (EDS) measurements done using a Hitachi, S-4800. The optical band gap was determined using a JASCO, V-670 UV−visible−NIR spectrophotometer. The cyclic voltammetric (CV) measurements for determining the band structure parameters were carried out using Metrohm potentiostat/galvanostat, Autolab PGSTAT 100 as per our recent studies.[3,25] The femtosecond transient absorption spectroscopy was carried out using HELIOS ultrafast setup.[26]

RESULTS AND DISCUSSION

XRD spectra of the $Cu_2Zn_{1-x}Cd_xSnS_4$ nanocrystals as shown in Figure 1a, reveal clear intense diffraction peaks, confirming their crystalline nature. The CZTS (x = 0) nanocrystals present in the kesterite (JCPDS No. 26-0575) shows diffraction peaks at 28.53°, 32.98°, 47.32°, and 56.17° which correspond to (112), (103), (200), and (220) plane orientations, respectively. We observe a transition from kesterite $Cu_2Zn_{1-x}Cd_xSnS_4$ to stannite (cernyite) phase after x = 0.6 of Cd exchange with Zn. The assigned stannite (cernyite) phase is confirmed by comparing our data to the standard JCPDS file (No. 26-0506). The CCTS (x = 1.0) nanocrystal shows diffraction peaks at 27.92°, 32.04°, 33.03°, 45.91°, 46.92°, 54.61°, and 55.99° which correspond to the (112), (200), (004), (220), (204), (312), and (116) crystal orientations.[12,13,24] Substitution of Zn^{2+} cation with Cd^{2+} resulted in a monotonic shift of the diffraction peaks toward small 2θ values, which indicate increasing lattice constants and unit cell volume with increasing Cd content. The increased unit cell parameters can be rationalized by considering the larger Cd^{2+} covalent radius (1.48 Å) compared to that of Zn^{2+} (1.25 Å). Bragg's equation was used to calculate the structural parameters, including the lattice parameters (a, b, c) and the interplanar spacing (d_{hkl}) (Table S1, Supporting Information). The average crystallite size (D_{hkl}) is calculated using the Scherrer equation ($D_{hkl} = k\lambda/\beta \cos\theta$),[27] where k is the shape factor, λ is the X-ray wavelength, β is the line broadening at half-maximum intensity, and θ is the Bragg's angle. The crystallite size of $Cu_2Zn_{1-x}Cd_xSnS_4$ is found to increase from 13.01 to 19.5 nm (Figure 1c) and the strain during cation substitution (Table S1, Supporting Information) decreases from 2.66×10^{-3} to 1.78×10^{-3}. Raman spectra (Figure 1b) confirm the phase purity of the $Cu_2Zn_{1-x}Cd_xSnS_4$ nanocrystals as no secondary phase was present. We have observed a linear shift in the Raman spectra (Figure 1b) with increasing Cd content toward lower wavenumbers, which confirms a gradual structural change from kesterite to stannite phase. Transmission electron microscopy pictures and the corresponding selected area electron diffraction (SAED) patterns recorded for CZTS and CCTS nanocrystals are shown in Figure 1c(i−vi). The TEM images (Figure 1c(i,iv)) show that the CZTS and CCTS nanocrystals are spherical in shape with diameter ranging from 15 to 25 nm. The HRTEM images (Figure 1c(ii,v)) specify CZTS and CCTS nanocrystals have lattice fringes with interplanar distance (d) of 0.312 and 0.319 nm, respectively, which are in good agreement with those determined from the diffraction peak in the XRD pattern (Table S1, Supporting Information). The SAED analysis of the CZTS and CCTS nanocrystals in Figure 1c(iii,vi) show concentric rings reflecting the polycrystalline nature of these materials. The room-temperature absorption spectra of the $Cu_2Zn_{1-x}Cd_xSnS_4$ nanocrystals (Figure 1d) disclose absorption in the entire visible area with a tail extending to the near-IR (NIR) region, giving rise to the black color of the samples. The inset in Figure 1d shows the subplot of $(\alpha h\nu)^2$ versus $(h\nu)$ for the $Cu_2Zn_{1-x}Cd_xSnS_4$ nanocrystals. We have observed a systematic decrease in the band gap from 1.51 to 1.03 eV for x = 0.0 to x = 1.0, as shown in Figure 1e and Table S2, Supporting Information. These results are consistent with a number of previous reports.[28−30] Ito et al. estimated the direct band gap of the (112) oriented polycrystalline films of CCTS and CZTS to be 1.06 and 1.46 eV, respectively.[31] From external quantum efficiency (EQE), Su et al. observed that when Cd content increases from 0 to 1.0, the band gaps of CZCTS thin films decrease first from 1.54 eV (CZTS) to 1.36 eV (CZCTS) and then increase to 1.41 eV (CCTS).[12] CCTS films prepared by Zhang et al. showed an estimated band gap in the range of 1.31−1.14 eV.[32] The differences reported in bandgaps by the various authors suggest that the bandgap of $Cu_2Zn_{1-x}Cd_xSnS_4$ is influenced by several factors including but not limited to film thickness, grain size, elemental composition, and defects.[3,10,15−17,25] The compositional analysis of the $Cu_2Zn_{1-x}Cd_xSnS_4$ nanocrystals was carried out using energy dispersive X-ray (EDS) analysis technique. The EDS data recorded in binding energy regions of 0−10 keV for the $Cu_2Zn_{1-x}Cd_xSnS_4$ nanocrystals (Table S3, Supporting Information) reveal that the Cu:Zn/Cd−Sn−S is close to the desired 2:1:1:4 ratio, hence our synthesis technique presents an accurate approach to carry out a controlled composition dependent synthesis, which is usually rather very challenging to achieve.

Further insights into the structural parameters, thermodynamic, and mechanical stabilities of the $Cu_2Zn_{1-x}Cd_xSnS_4$(x = 0.0, 0.25, 0.50, 0.75, and 1.00) materials was gained through first-principles DFT calculations. The structures at x = 0.0 (CZTS) and x = 1.0 (CCTS) compositions are shown in Figure 2a,d, which are modeled in their most stable kesterite

https://dx.doi.org/10.1021/acsaem.9b02314
ACS Appl. Energy Mater. 2020, 3, 5153−5162

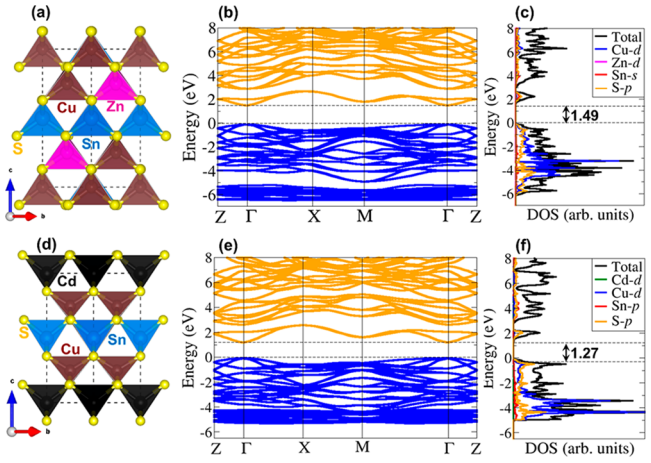

Figure 2. Crystal structure of (a) kers-Cu_2ZnSnS_4 and (d) stan-Cu_2CdSnS_4. The HSE06 band structure (b,e) and the corresponding DOS of (c,f) of kers-Cu_2ZnSnS_4 and stan-Cu_2CdSnS_4, respectively. The Fermi level has been set to zero.

and stannite structures, respectively. The intermediate x = 0.25, 0.50, and 0.75 systems are shown in Supporting Information Figure S2. The calculated lattice constants and lattice spacing are found to increase with increasing Cd concentration, which is in good agreement with the experimentally measured ones, as shown in Table S4 (Supporting Information). The cohesive energy, which gives a measure of the stability of the studied materials, has been evaluated for the different Cd compositions in $Cu_2Zn_{1-x}Cd_xSnS_4$. The cohesive energy of CZTS is found to be 4.036 eV/atom, which closely agrees with the experimentally reported[33] value of 3.9 eV/atom and is comparable to that of bulk silicon (expt., 4.68 eV/atom). A gradual decrease in cohesive energy with increasing Cd content in the unit cell is observed (Table S5, Supporting Information). However, all compositions show comparable cohesive energies ranging from 3.943 to 4.036 eV/atom, indicating that Cd does not significantly affect the thermodynamic stability in $Cu_2Zn_{1-x}Cd_xSnS_4$ materials. To ascertain the mechanical stability of these systems, their bulk elastic parameters, such as bulk modulus, shear modulus, Young's modulus, and Poisson's ratio at x = 0.0, 0.5, and 1.0 compositions have been calculated, which are tabulated in Table S6 (Supporting Information). All of the calculated single-crystal elastic constants provided in Table S6 are found to satisfy the Born-Huang's mechanical stability criteria for tetragonal structures[34] thereby confirming the mechanical stability in the studied materials under ambient conditions. The bulk and Young's moduli of CZTS are calculated to be 75.5 and 78.9 GPa, respectively, as compared to CCTS values of 62.5 and 64.4 GPa, respectively. The bulk to shear modulus ratios are found to be greater than 1.75 for all the compositions, thus establishing the ductility of the studied $Cu_2Zn_{1-x}Cd_xSnS_4$ materials. Also, the calculated Poisson's ratio (<0.5) substantiates their stability against shear.

To examine the result of Cd substitution on electronic structures of the $Cu_2Zn_{1-x}Cd_xSnS_4$ materials, we have calculated the electronic band structures and partial density of states (PDOS) of the different compositions using the hybrid exchange-correlation functional (HSE06), which has been shown to give a good description of the electronic properties of CZTS.[35−38] It is quite evident from the band structure of the $Cu_2Zn_{1-x}Cd_xSnS_4$ materials (x = 0.0 and x = 1.0) as shown in Figure 2b,e, and other compositions (Figure S3, Supporting Information)) that the $Cu_2Zn_{1-x}Cd_xSnS_4$ materials are direct band gap semiconductors as both the valence band maxima and conduction band minima possess similar momentum position and lie in high-symmetry Γ-point. A reduction in the bandgap with increasing Cd concentration was first observed (x = 0−0.75, that is, from 1.49 eV (CZTS) to 1.10 eV (CZCTS)) and then an increase to 1.27 eV for CCTS (x = 1). These results are consistent with previous theoretical predictions[35−38] and experimental characterization

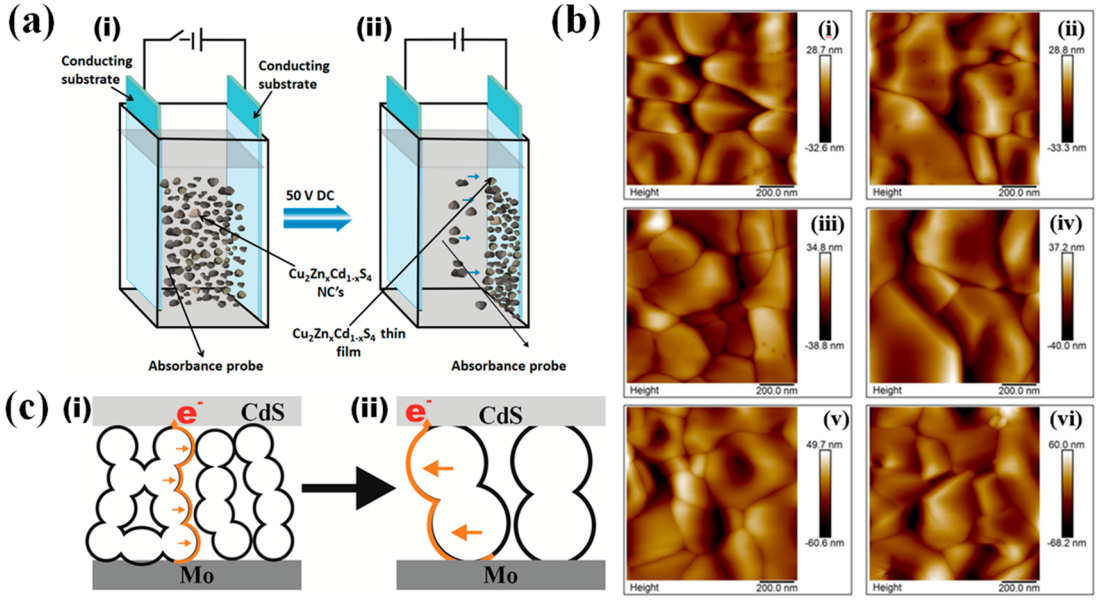

Figure 3. (a) Schematic diagram illustrating the thin film deposition for $Cu_2Zn_{1-x}Cd_xSnS_4$ nanocrystals. (b) Images (i−vi) represent two-dimensional (2D) AFM images for $Cu_2Zn_{1-x}Cd_xSnS_4$ thin films with 1 μm^2 surface areas. (c) Schematic diagram showing how the grain size of the $Cu_2Zn_{1-x}Cd_xSnS_4$ thin film will influence charge carrier separation.

https://dx.doi.org/10.1021/acsaem.9b02314
ACS Appl. Energy Mater. 2020, 3, 5153−5162

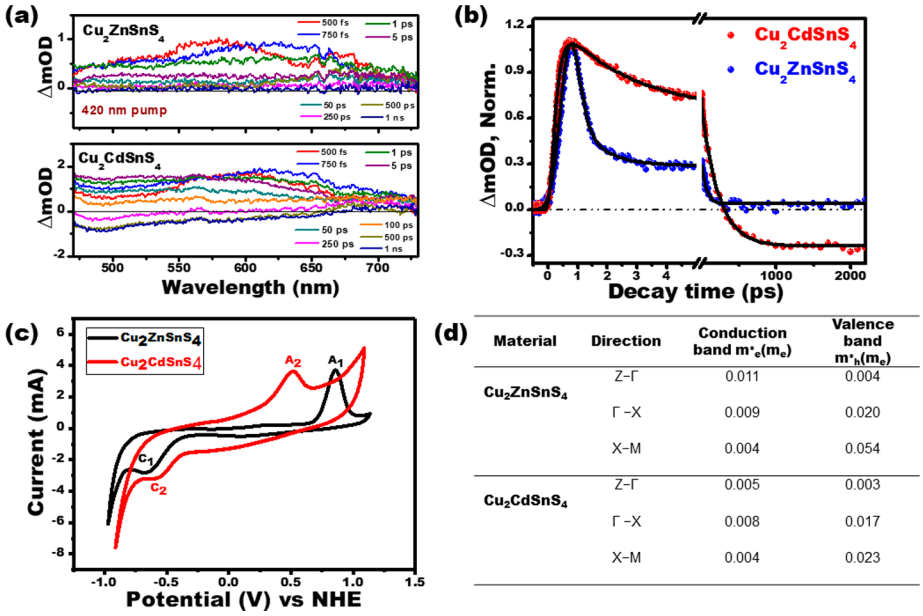

Material	Direction	Conduction band $m^*_e(m_e)$	Valence band $m^*_h(m_e)$
Cu_2ZnSnS_4	Z–Γ	0.011	0.004
	Γ –X	0.009	0.020
	X–M	0.004	0.054
Cu_2CdSnS_4	Z–Γ	0.005	0.003
	Γ –X	0.008	0.017
	X–M	0.004	0.023

Figure 4. (a) Differential transient absorption spectrum of CZTS and CCTS nanocrystals at different pump–probe delay time following 420 nm photoexcitation. (b) Normalized transient absorption kinetics CZTS and CCTS NCs at similar experimental conditions. (c) Cyclic voltammograms for CZTS and CCTS nanocrystals. (d) Effective masses of electrons (conduction band) and holes (valence band) of Cu_2ZnSnS_4 and Cu_2CdSnS_4 along high symmetry directions.

of solution-processed Cd-substituted CZTS materials.[12,13] The partial density of states of Cu_2ZnSnS_4 and Cu_2CdSnS_4 in Figure 2(c,f) indicates that the valence band maximum (VBM) of both materials is composed mainly of Cu-3d and S-3p states. The conduction band minimum (CBM) on the other hand is composed primarily of Sn-5s and S-3p states. Considering that the optical absorption properties of a semiconductor are of great importance in its photovoltaic activity, we have simulated the absorption spectra of the $Cu_2Zn_{1-x}Cd_xSnS_4$ materials, as shown in Supporting Information in Figure S4. A high absorption coefficient ($\alpha_{abs} > 10^5$ cm^{-1}) is predicted for the $Cu_2Zn_{1-x}Cd_xSnS_4$ materials, which agrees very well with experimental results. The red shift in the absorption peak with increasing Cd concentration is consistent with the trends observed in the experimental UV–visible–NIR optical absorption spectra. These properties show great promise for $Cu_2Zn_{1-x}Cd_xSnS_4$ in multijunction tandem solar cells.

Next, to investigate the topological properties, we have developed a unique and simple electrophoretic deposition method to successfully deposit highly dense and uniform $Cu_2Zn_{1-x}Cd_xSnS_4$ thin films. Shown in Figure 3a, is the schematic diagram illustrating the deposition process for $Cu_2Zn_{1-x}Cd_xSnS_4$ thin films. In the setup, DC power was used to apply the potential to two FTO electrodes dipped into $Cu_2Zn_{1-x}Cd_xSnS_4$ nanocrystals solution. The working and counter bare FTO electrodes were introduced in parallel with ∼7 mm gap in 5 mg/mL $Cu_2Zn_{1-x}Cd_xSnS_4$ nanocrystal solution. After systematic optimization of the applied voltage to 50 V and increasing the deposition time to 45 min, the suspended nanocrystals in the solution moved toward the positive electrode to form highly dense and uniform thin films. The surface properties of the $Cu_2Zn_{1-x}Cd_xSnS_4$ films were examined by atomic force microscopy (AFM). Two-dimensional (2D) AFM micrographs (Figure 3b) were obtained without any additional or postannealing treatment. The three-dimensional (3D) surface topology of the $Cu_2Zn_{1-x}Cd_xSnS_4$ films were evaluated for 1 μm^2 surface areas (Supporting Information Figure S1), which revealed a smooth and highly homogeneous thin film with low surface roughness within 10–20 nm range (Table S7, Supporting Information). The magnified AFM images (Figure 3b) confirm the formation of $Cu_2Zn_{1-x}Cd_xSnS_4$ thin films with grain sizes in the range of 50–400 nm. Similar large grain sizes were reported by Badkoobehhezaveh et al.[39] from their SEM micrographs of $CZT(S_xSe_{1-x})_4$ films fabricated by electrophoretic deposition technique without postannealing. Ravi et al.[40] employed a similar deposition procedure with an applied voltage of 100 V to achieve the deposition of larger linear rods (∼500 nm in length) of cesium lead halide perovskite nanocrystals without postannealing. The effect of the annealing temperature on the formation of Cu_2ZnSnS_4 thin films has been investigated by several authors who have all achieved large grain (micron-sized grains) with sulfurization treatments.[41−46] The obtained large grains in the present study may facilitate carrier transport and easy collection, thus improving device performance via minimizing trapping and recombination of photogenerated carriers. In Figure 3c, we provide a schematic diagram showing how larger grain can enhance charge carrier transport and reduce carrier trapping at grain boundaries in thin films compared to smaller grain size. With smaller grain sizes (Figure 3c(i)), the probability of recombination will be high at grain boundaries whereas with larger grain sizes (Figure 3c(i)), the recombination of charge carries can be significantly minimized.

To gain insight into the native photophysics in CZTS and CCTS systems, we have employed ultrafast pump–probe spectroscopy with 420 nm pump excitation and probed the transients in the visible region of the spectrum. The transient spectra (TA) manifest a broad photoinduced absorption band throughout the visible region (450–760 nm), represented in Figure 4a. This positive feature in the case of CZTS persists along the temporal evolution of the spectra for the entire time range until it completely decays. Interestingly, the TA spectra of CCTS nanocrystals show positive absorption band until 200 ps, but beyond 250 ps a negative absorption band (bleach)

https://dx.doi.org/10.1021/acsaem.9b02314
ACS Appl. Energy Mater. 2020, 3, 5153–5162

appears in the 450−650 nm region which exists beyond 2 ns. The photoinduced transient absorption is found to dominate the TA spectra for both CZTS and CCTS nanocrystals. The transient kinetics of charge carriers near the photoinduced absorption maxima (600 nm) for the CZTS and CCTS nanocrystals was also monitored as shown in Figure 4b. It is interesting to see that the nature of the kinetic traces for CZTS and CCTS nanocrystals is completely different. The transient kinetics was fitted multiexponentially and fitting parameters are listed in Supporting Information Table S8. The transient kinetics for CZTS NCs is composed of 190 fs growth time component and three decay time scales being τ_1 = 0.38 ps (−64.4%), τ_2 = 72.1 ps (−31.9%), and τ_3 = > 2 ns (−3.7%). Similarly, the multiexponential fitting parameters for CCTS transient kinetics are 130 fs growth time and three decay time constants being, τ_1 = 3.48 ps (−44.1%), τ_2 = 247 ps (−55.9%), and τ_3 = >2 ns (+100%), respectively. We observed that the majority of the CZTS photoinduced feature depletes at a much faster rate (τ_1^{CZTS} = 0.38 ps) compared to CCTS (τ_1^{CCTS} = 3.48 ps). One may attribute this faster transient decay of CZTS due to quicker trapping of photoexcited charge carriers in the CZTS system compared to that of CCTS. It has also been observed that the transient positive signal of CZTS completely decays within 2 ns. However, in the case of CCTS at longer time scale (beyond 250 ps onward), the bleach signal appears which matches with optical absorption band of CCTS (Figure 4b). The existence of the bleach signal beyond 2 ns clearly suggests that the charge carriers generated in CCTS are much longer lived as compared to that of CZTS. Our results are similar to those obtained by Pundsack et al. who reported short excited state lifetime (<20 ps) of the photoexcited charge carrier for CZTS nanocrystal[47] and unfavorable nonradioactive recombinations of the carrier's limit efficiency in solar cells. Our spectroscopic measurement indicates the more efficient separation of optically excited charge carriers leading into slower electron−hole recombination in CCTS as compared to CZTS nanocrystals. Consistent with our spectroscopic study, previous reports have observed enhanced current density and solar power conversion efficiency for $Cu_2Zn_{1-x}Cd_xSnS_4$ device as compare to pure CZTS.[12,13,24]

The mean effective mass of charge carriers influences their transport properties; hence, we have calculated the hole and electron mean effective masses for CZTS and CCTS. A quadratic polynomial was fitted to the energy of the corresponding bands in the reciprocal lattice vector **k** for this calculation. The calculated electron and hole effective masses for CZTS and CCTS NC's in some selective directions of the Brillouin zone are shown in Figure 4d. Such light mass charge carriers can be easily separated due to photoexcitation and can enhance the efficiency of solar cell devices. The slightly smaller electron and hole effective masses calculated for CCTS in almost all directions than CZTS suggest higher charge carrier mobility (electrical conductivity). In line with this, recent studies by Wong and co-workers have reported efficiency improvement for Cd-substitution with Zn (η = 9%)[12] and double cation (Cd for Zn and Ag for Cu) substitution (η = 10%)[13] for CZTS solar cells.

The band edges (VBM and CBM) of the CZTS and CCTS were determined through cyclic voltammetry measurements (scan rate, 100 mV s^{-1}). This measurement permits the estimation of the electrochemical bandgap and the electron affinity (EA) of CZTS and CCTS. Figure 4c shows the CV data for CZTS with two peaks marked as A_1 and C_1 at 0.85 V (−5.35 V vs V_{ac}) and at −0.68 V (−3.82 V vs V_{ac}) over repeated cycles, which correspond to the anodic and cathodic peaks, respectively. For CCTS, the anodic A_2 and cathodic C_2 peaks are observed at 0.51 V (−5.01 V vs V_{ac}) and at −0.6 V (−3.9 V vs V_{ac}), respectively. The potential difference between the anodic and cathodic peaks of CZTS (1.53 V) and CCTS (1.11 V) corresponds to their bandgap values. CdS, which is commonly used as a buffer layer for CZTS PV devices has a band gap of 2.42 eV and electron affinity of 4.0 eV.[48] The exact positions of the conduction and valence bands with respect to the vacuum level are calculated using the relations E_{VBM} = −IP = −($E_{peak\text{-}oxidation}$ + E_{ref}) and E_{CBM} = −EA = −($E_{peak\text{-}reduction}$ + E_{ref}), where IP is the ionization potential and EA is the electron affinity.[1] Ferrocene was used as the internal reference E_{ref} (4.5 eV vs NHE), and $E_{peak\text{-}oxidation}$ and $E_{peak\text{-}reduction}$ energies corresponds to A_1 and C_1 peaks, respectively, in Figure 4c. On the basis of the estimated IP and EA values, the band alignment of the CZTS/CdS and CCTS/CdS heterojunctions was constructed (Figure 5), showing a staggered type II band

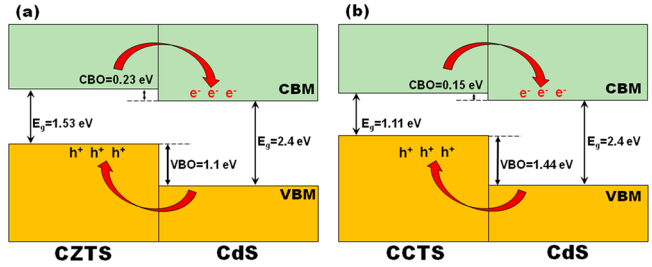

Figure 5. Energy band alignment diagram of (a) CZTS/CdS and (b) CCTS/CdS heterojunctions

alignment. The conduction band offset (CBO) and valence band offset (VBO) of the CZTS/CdS heterostructure are estimated at 0.23 and 1.10 eV, respectively, whereas for CCTS/CdS heterostructure, they are 0.15 and 1.44 eV, respectively.

The CZTS/CdS and CCTS/CdS interfaces were simulated in order to derive atomic-level insights about the interface structures, composition, stabilities, and band offsets. From the band structure and density of states of CdS provided in Supporting Information, Figure S5, the band gap is predicted at 2.45 eV. A (2 × 2) CZTS or CCTS supercell and a (3 × 2) CdS supercell were used to construct the CZTS/CdS and CCTS/CdS heterojunctions, ensuring less than 5% lattice mismatch. The optimized structure of the CZTS(001)/CdS(100) and CCTS(001)/CdS(100) heterojunctions are shown in Figure 6a,c and the corresponding energy band alignment diagrams are illustrated in Figure 6b,d. The two interfaces are found to be dominated by strong covalent Cu−S and Cd−S interactions, which are calculated at 2.229 and 2.578 Å at the CZTS/CdS interface compared to 2.284 and 2.631 Å at the CCTS/CdS interface. The interfacial adhesion energy, calculated as E_{ad} = ($E_{A/B}$ − (E_A + E_B))/S, where E_A and E_B are the individual ground-state relaxed total energy of layer A and layer B, respectively, is used to evaluate the thermodynamic stability of the heterojunctions. $E_{A/B}$ is the total energy of the entire A/B interface system calculated based on the geometry optimized structure and S is the surface area of the interface. The adhesion energy of the CZTS(001)/CdS(100) and CCTS(001)/CdS(100) heterostructures was calculated to be −0.189 eV $Å^{-2}$ and −0.149 eV $Å^{-2}$,

https://dx.doi.org/10.1021/acsaem.9b02314
ACS Appl. Energy Mater. 2020, 3, 5153−5162

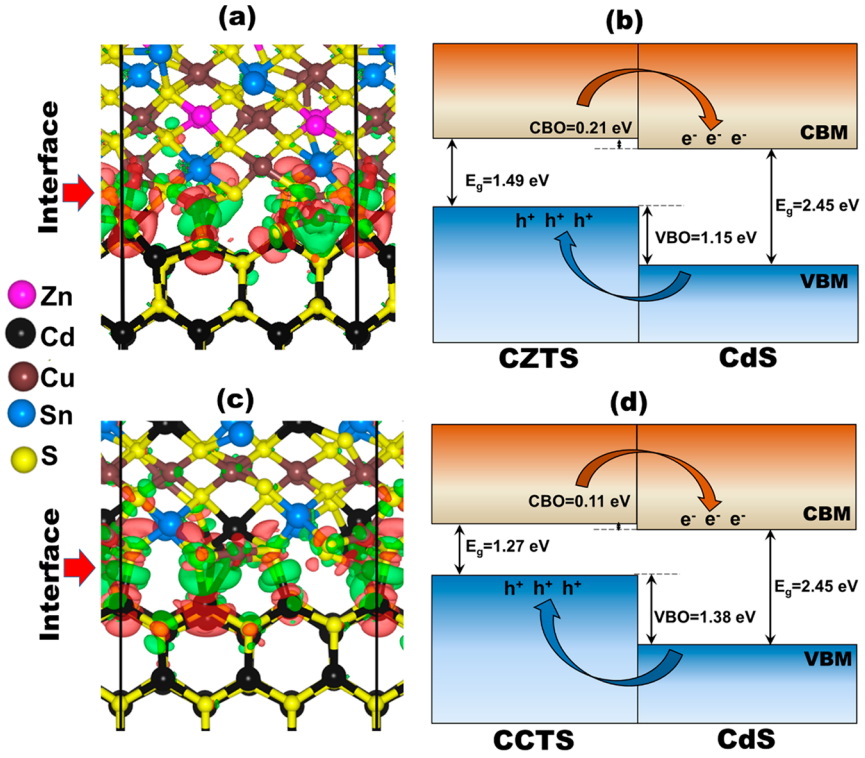

Figure 6. Geometry optimized model of the (a) CZTS(001)/CdS(100) and (c) CCTS(001)/CdS(100) interface. The corresponding isosurface of the differential charge densities at the interface the red (charge depletion) and green (charge accumulation) contours. Schematic representation of the valence-band offset (VBO) and the conduction-band offset (CBO) are shown in panels b and d.

respectively, which indicates both interfaces are stable. The interfaces are stabilized by newly formed Cu−S and Cd−S chemical bonds, confirmed by electron density accumulation in these boding regions. By applying the potential-line-up method according to the formula: BO = $\Delta E_{v,c} + \Delta V$, where ΔE_v refers to the difference in the VBM, the band offsets (BOs) at the heterojunction interfaces were calculated. ΔV results from the line-up of the macroscopic average of the self-consistent electrostatic potential across the interface. By solving the Poisson equation, the electrostatic potential $V(\bar{r})$ and the planar-averaged potential $\overline{V}(z)$ of the heterojunctions can be obtained from the equation $\overline{V}(z) = \frac{1}{S}V(\bar{r})\mathrm{d}x\ \mathrm{d}y$, where S is the interface surface area. Employed as a reference level to align the valence-band, the macroscopic average of electrostatic potential $\overline{\overline{V}}(z)$ was calculated as $\overline{\overline{V}}(z) = \frac{1}{L}\int_{-L/2}^{L/2}\overline{V}(z')\mathrm{d}z'$, where L is a corresponding distance of one period at each point z'. The planar-averaged electrostatic potential of the CZTS/CdS and CCTS/CdS heterojunctions are shown in Figures S6 and S7. By adding calculated band gaps to the relative position of the valence bands, the discontinuities at the conduction band can be obtained as $\Delta E_c = \Delta E_v + \Delta E_g$. The schematic representation of the predicted band discontinuities for the CZTS/CdS and CCTS/CdS heterostructures are shown in Figure 6b,d, both of which reveal type II staggered band alignment. The CBO and VBO at the CZTS/CdS interface are 0.21 and 1.15 eV, respectively, compared to 0.11 and 1.38 eV at the CCTS/CdS interface. These results are consistent with the experimental CV measurements and point to efficient charge separation with photoexcited electrons migrating to the buffer CdS layer and holes to the absorber CZTS or CCTS layer.

In a working PV device, the electron and the hole have to be dissociated to obtain free charge carriers. The exciton is characterized by its binding energy (E_b) and it has to be as low as possible to facilitate the dissociation. If we assume that the exciton will be dissociated by the thermal energy, E_b should be lower than k_BT (around 25 meV at room temperature). After the free charge carriers are created from the exciton dissociation step, they have to diffuse to the back electrodes in a photovoltaic system before their recombination. The discontinuities at the absorber/buffer interface act as barriers to electrical transport across the interface. Hence the magnitude of the discontinuities (band offsets) controls the transport phenomena at these interfaces and characteristics of devices. The smaller the CBO and the VBO between the absorber/buffer layers the less resistance the free charge carriers experience when moving across the interfaces. This often results in efficient free charge carrier separation and minimized recombination rates. In light of this, the smaller CB offset predicted for the CCTS/CdS compared to the CZTS/CdS indicates that free electrons generated in CCTS will diffuse much faster and be collected before their recombination with free holes in the VB. Consistent with our results, recent studies have reported higher efficiencies for $Cu_2Zn_{1-x}Cd_xSnS_4$ based devices than pure CZTS.[12,13,24]

CONCLUSIONS

In summary, we have employed combined experimental and theoretical approaches to unravel the interface chemistry and energy band alignment of $Cu_2Zn_{1-x}Cd_xSnS_4$ based heterointerface. Insight into the charge carrier dynamics of the CZTS and CCTS nanocrystal are also provided. Without any postannealing treatment, highly dense and uniform $Cu_2Zn_{1-x}Cd_xSnS_4$ thin films with large gains were obtained using electrophoretic

https://dx.doi.org/10.1021/acsaem.9b02314
ACS Appl. Energy Mater. 2020, 3, 5153−5162

deposition method. Besides exhibiting high absorption coefficient ($\sim 10^5$ cm^{-1}), we have observed bandgap tuning (1.51−1.02 eV) of the $Cu_2Zn_{1-x}Cd_xSnS_4$ with increasing Cd concentration, which is promising for highly efficient solar cell fabrication. A type-II staggered band alignment was observed at the CZTS/CdS and CCTS/CdS heterointerfaces with a smaller conduction band offset of 0.15 eV (0.11 from DFT) predicted for the CZTS/CdS as compared to 0.23 eV (0.21 from DFT) for the CZTS/CdS interface. The observed type-II staggered band alignment points to efficient charge separation and transfer across the interfaces and ultrafast transient spectroscopic measurements show longer charge carrier lifetime in CCTS as compared to CZTS nanocrystal. These results provide detailed insights into recent reports of enhancement of the photocurrent in Cd-substituted CZTS devices, which we have shown can be ascribed primarily to optimal band gap tuning, improved band offsets, and long-lived charge carriers in CCTS compared to CZTS. The controlled deposition of large grain $Cu_2Zn_{1-x}Cd_xSnS_4$ thin films at room temperature with favorable optoelectronic properties should open novel paths for evolving additional effective Cu-quaternary chalcogenides-based solar cells and flexible display devices.

■ ASSOCIATED CONTENT

Supporting Information

The Supporting Information is available free of charge at https://pubs.acs.org/doi/10.1021/acsaem.9b02314.

Figures showing computational details, atomic force microscopy (AFM) analysis, transient absorption spectrum, crystal structure of $Cu_2Zn_{1-x}Cd_xSnS_4$(DFT), DFT simulated absorption spectra, crystal structure, band structure and projected density states of the hexagonal CdS, optimized strucutures of the CdS(100)/CZTS(001) and CdS(100)/CCTS(001) heterojucntions with their corresponding electrostatic potentials. Tables show structural analysis (lattice parameters, interplanar distance, crystallite size, and strain), optical bandgap (experimental and theory), EDS analysis, simulated (theory) lattice parameters (*a*, *b*, and *c*), cohesive energy, elastic properties, AFM analysis surface roughness of the $Cu_2Zn_{1-x}Cd_xSnS_4$ thin films, exponentially fitted parameters from transient spectroscopy data (PDF)

■ AUTHOR INFORMATION

Corresponding Author

Hirendra N. Ghosh − *Institute of Nano Science and Technology, Mohali, Punjab 160062, India;* orcid.org/0000-0002-2227-5422; Phone: +91-172-2210075/57/56 ext. 120; Email: hnghosh@inst.ac.in; Fax: +91-172-2211074

Authors

Sachin R. Rondiya − *Institute of Nano Science and Technology, Mohali, Punjab 160062, India;* orcid.org/0000-0003-1350-1237

Yogesh Jadhav − *Department of Chemistry, Savitribai Phule Pune University, Pune 411007, India*

Nelson Y. Dzade − *School of Chemistry, Cardiff University, Cardiff CF10 3AT, Wales, United Kingdom;* orcid.org/0000-0001-7733-9473

Raihan Ahammed − *Institute of Nano Science and Technology, Mohali, Punjab 160062, India*

Tanmay Goswami − *Institute of Nano Science and Technology, Mohali, Punjab 160062, India*

Abir De Sarkar − *Institute of Nano Science and Technology, Mohali, Punjab 160062, India;* orcid.org/0000-0001-5752-6589

Sandesh Jadkar − *Department of Physics, Savitribai Phule Pune University, Pune 411007, India*

Santosh Haram − *Department of Chemistry, Savitribai Phule Pune University, Pune 411007, India;* orcid.org/0000-0002-0618-1215

Complete contact information is available at: https://pubs.acs.org/10.1021/acsaem.9b02314

Notes

The authors declare no competing financial interest.

■ ACKNOWLEDGMENTS

S.R.R acknowledges the Institute of Nano Science and Technology (INST), Department of Science and Technology, Government of India for financial support under "Institute Postdoctoral Fellowship". H.N.G. is grateful to DST, Government of India, for JC Bose fellowship (JCB/2018/000047) and SERB/DST (CRG/2019/000938). Y.A.J. thanks DST INSPIRE Ph.D. program (Grant 2013/606) and SPPU PDF program for the financial support. N.Y.D. acknowledges the U.K. Engineering and Physical Sciences Research Council (EPSRC) for funding (Grant EP/S001395/1). A.D.S. and R.A. gratefully acknowledge Grant SR/NM/NS-1125/2016(G) from DST (Nanomission) and CDAC-Pune's supercomputing resources on PARAM Yuva II & PARAM Shavak HPC system at INST. This work has also used the computational facilities of the Advanced Research Computing at Cardiff (ARCCA) Division, Cardiff University, and HPC Wales. The authors thank Dr. Radhamanohar Aepuru, Nandan Ghorai, and Gurpreet Kaur for their support during the work.

■ REFERENCES

(1) Wadia, C.; Alivisatos, A. P.; Kammen, D. M. Materials availability expands the opportunity for large-scale photovoltaics deployment. *Environ. Sci. Technol.* **2009**, *43* (6), 2072−2077.

(2) Alharbi, F.; Bass, J. D.; Salhi, A.; Alyamani, A.; Kim, H.; Miller, R. Abundant non-toxic materials for thin film solar cells: Alternative to conventional materials. *Renewable Energy* **2011**, *36*, 2753−2758.

(3) Rondiya, S.; Wadnerkar, N.; Jadhav, Y.; Jadkar, S.; Haram, S.; Kabir, M. Structural, electronic, and optical properties of Cu_2NiSnS_4: A combined experimental and theoretical study toward photovoltaic applications. *Chem. Mater.* **2017**, *29*, 3133−3142.

(4) Shockley, W.; Queisser, H. J. Detailed balance limit of efficiency of *pn* junction solar Cells. *J. Appl. Phys.* **1961**, *32*, 510−519.

(5) Gour, K. S.; Singh, O. P.; Bhattacharyya, B.; Parmar, R.; Husale, S.; Senguttuvan, T. D.; Singh, V. N. Enhanced photoresponse of $Cu_2ZnSn(S, Se)_4$ based photodetector in visible range. *J. Alloys Compd.* **2017**, *694*, 119−123.

(6) Wang, L.; Wang, W.; Sun, S. A simple template-free synthesis of ultrathin Cu_2ZnSnS_4 nanosheets for highly stable photocatalytic H_2 evolution. *J. Mater. Chem.* **2012**, *22*, 6553−6555.

(7) Ha, E.; Lee, L. Y. S.; Wang, J.; Li, F.; Wong, K. Y.; Tsang, S. C. E. Significant enhancement in photocatalytic reduction of water to hydrogen by Au/Cu_2ZnSnS_4 nanostructure. *Adv. Mater.* **2014**, *26*, 3496−3500.

(8) Sarswat, P. K.; Free, M. L. Demonstration of a sol−gel synthesized bifacial CZTS photoelectrochemical cell. *Phys. Status Solidi A* **2011**, *208*, 2861−2864.

(9) Lin, J.; Guo, J.; Liu, C.; Guo, H. Three-dimensional Cu_2ZnSnS_4 films with modified surface for thin-film lithium-ion batteries. *ACS Appl. Mater. Interfaces* **2015**, *7*, 17311−17317.
(10) Kumar, M.; Dubey, A.; Adhikari, N.; Venkatesan, S.; Qiao, Q. Strategic review of secondary phases, defects and defect-complexes in kesterite CZTS−Se solar cells. *Energy Environ. Sci.* **2015**, *8*, 3134−3159.
(11) Wang, W.; Winkler, M. T.; Gunawan, O.; Gokmen, T.; Todorov, T. K.; Zhu, Y.; Mitzi, D. B. Mitzi, D. B. Device characteristics of CZTSSe Thin-Film Solar Cells with 12.6% Effi ciency. *Adv. Energy Mater.* **2014**, *4*, 1301465.
(12) Su, Z.; Tan, J. M. R.; Li, X.; Zeng, X.; Batabyal, S. K.; Wong, L. H. Cation substitution of solution-processed Cu_2ZnSnS_4 thin film solar cell with over 9% Efficiency. *Adv. Energy Mater.* **2015**, *5*, 1500682.
(13) Hadke, S. H.; Levcenko, S.; Lie, S.; Hages, C. J.; Márquez, J. A.; Unold, T.; Wong, L. H. Synergistic effects of double cation substitution in solution-processed CZTS solar cells with over 10% efficiency. *Adv. Energy Mater.* **2018**, *8*, 1802540.
(14) Yun, H. J.; Paik, T.; Edley, M. E.; Baxter, J. B.; Murray, C. B. Enhanced charge transfer kinetics of CdSe quantum dot-sensitized solar cell by inorganic ligand exchange treatments. *ACS Appl. Mater. Interfaces* **2014**, *6*, 3721−3728.
(15) Ma, Y.; Li, W.; Feng, Y.; Li, Z.; Ma, X.; Liu, X.; Wu, X.; Zhang, Y.; Yang, C.; Lu, X.; Wang, K.; Xiao, X. Band bending near grain boundaries of $Cu_2ZnSn(S, Se)_4$ thin films and its effect on photovoltaic performance. *Nano Energy* **2018**, *51*, 37−44.
(16) Wei, Y.; Zhuang, D.; Zhao, M.; Gong, Q.; Sun, R.; Ren, G.; Wu, Y.; Zhang, L.; Lyu, X.; Peng, X.; Wei, J. An investigation on the relationship between open circuit voltage and grain size for CZTSSe thin film solar cells fabricated by selenization of sputtered precursors. *J. Alloys Compd.* **2019**, *773*, 689−697.
(17) Yan, Y.; Jiang, C. S.; Noufi, R.; Wei, S. H.; Moutinho, H. R.; Al-Jassim, M. M. Electrically benign behavior of grain boundaries in polycrystalline $CuInSe_2$ films. *Phys. Rev. Lett.* **2007**, *99*, 235504.
(18) Maity, P.; Maiti, S.; Debnath, T.; Dana, J.; Guin, S. K.; Ghosh, H. N. Intraband electron cooling mediated unprecedented photocurrent conversion efficiency of CdSxSe1-x Alloy QDs: direct correlation between electron cooling and efficiency. *J. Phys. Chem. C* **2016**, *120*, 21309−21316.
(19) Debnath, T.; Parui, K.; Maiti, S.; Ghosh, H. N. An insight into the interface through excited-state carrier dynamics for promising enhancement of power conversion efficiency in a Mn-doped CdZnSSe gradient alloy. *Chem. - Eur. J.* **2017**, *23*, 3755−3763.
(20) Dana, J.; Anand, P.; Maiti, S.; Azlan, F.; Jadhav, Y.; Haram, S. K.; Ghosh, H. N. Inhibiting interfacial charge recombination for boosting power conversion efficiency in CdSe{Au} nanohybrid sensitized solar cell. *J. Phys. Chem. C* **2018**, *122*, 13277−13284.
(21) Dana, J.; Maiti, S.; Tripathi, V. S.; Ghosh, H. N. Direct correlation of excitonics with efficiency in a core−shell quantum dot solar cell. *Chem. - Eur. J.* **2018**, *24*, 2418−2425.
(22) Maiti, S.; Dana, J.; Ghosh, H. N. Correlating charge-carrier dynamics with efficiency in quantum-Dot Solar Cells: Can Excitonics Lead to Highly Efficient Devices? *Chem. - Eur. J.* **2019**, *25*, 692−702.
(23) Seto, J. Y. W. The electrical properties of polycrystalline silicon films. *J. Appl. Phys.* **1975**, *46*, 5247.
(24) Yan, C.; Sun, K.; Huang, J.; Johnston, S.; Liu, F.; Veettil, B. P.; Sun, K.; Pu, A.; Zhou, F.; Stride, J. A.; Green, M. A.; Hao, X. Beyond 11% efficient sulfide kesterite $Cu_2ZnxCd_{1-x}SnS_4$ solar cell: effects of cadmium alloying. *ACS Energy Lett.* **2017**, *2*, 930−936.
(25) Jadhav, Y. A.; Thakur, P. R.; Haram, S. K. Voltammetry investigation on copper zinc tin sulphide /selenide ($CZTS_xSe_{1-x}$) alloy nanocrystals: Estimation of composition dependent band edge parameters. *Sol. Energy Mater. Sol. Cells* **2016**, *155*, 273−279.
(26) Aepuru, R.; Mondal, S.; Ghorai, N.; Kumar, V.; Panda, H. S.; Ghosh, H. N. Exploring the carrier dynamics in zinc oxide-metal halide-based perovskite nanostructures: toward reduced dielectric loss and improved photocurrent. *J. Phys. Chem. C* **2018**, *122*, 27273−27283.
(27) Williamson, G.; Smallman, R. Dislocation densities in some annealed and cold-worked metals from measurements on the X-ray debyescherrer spectrum. *Philos. Mag.* **1956**, *1*, 34−46.
(28) Xiao, Z.; Li, Y.; Yao, B.; Deng, R.; Ding, Z.; Wu, T.; Yang, G.; Li, C.; Dong, Z.; Liu, L.; Zhang, L.; Zhao, H. Bandgap engineering of $Cu_2Cd_xZn_{1-x}SnS_4$ alloy for photovoltaic applications: A complementary experimental and first-principles study. *J. Appl. Phys.* **2013**, *114*, 183506.
(29) Xu, N.; Li, P.; Hao, Y.; Wang, X.; Meng, L. Effect of sputtering power on Cd/Zn atomic ratio and optical properties of $Cu_2Zn_xCd_{1-x}SnS_4$ thin films deposited by magnetron sputtering: An experimental and first-principle study. *Chem. Phys. Lett.* **2016**, *660*, 132−135.
(30) Pilvet, M.; Kauk-Kuusik, M.; Altosaar, M.; Grossberg, M.; Danilson, M.; Timmo, K.; Mere, A.; Mikli, V. Compositionally tunable structure and optical properties of $Cu_{1.85}(Cd_xZn_{1-x})_{1.1}SnS_{4.1}$ ($0 \le x \le 1$) monograin powders. *Thin Solid Films* **2015**, *582*, 180−183.
(31) Ito, K.; Nakazawa, T. Electrical and optical properties of stannite-type quaternary semiconductor thin films. *Jpn. J. Appl. Phys.* **1988**, *27*, 2094−2097.
(32) Zhang, Q.; Deng, H.; Chen, L.; Tao, J.; Yu, J.; Yang, P.; Chu, J. Effects of sulfurization temperature on the structural and optical properties of Cu_2CdSnS_4 thin films prepared by direct liquid method. *Mater. Lett.* **2017**, *193*, 206−209.
(33) Baryshev, S. V.; Thimsen, E. Enthalpy of formation for Cu-Zn-Sn-S (CZTS) calculated from surface binding energies experimentally measured by ion sputtering. *Chem. Mater.* **2015**, *27*, 2294−2298.
(34) Mouhat, F.; Coudert, F. X. Necessary and sufficient elastic stability conditions in various crystal systems. *Phys. Rev. B: Condens. Matter Mater. Phys.* **2014**, *90*, 4−7.
(35) Chen, S.; Walsh, A.; Gong, X.-G.; Wei, S.-H. Classifi cation of lattice defects in the kesterite Cu_2ZnSnS_4 and $Cu_2ZnSnSe_4$ earth-abundant solar cell absorbers. *Adv. Mater.* **2013**, *25*, 1522−1539.
(36) Kim, S.; Park, J.; Walsh, A. Identification of killer defects in kesterite thin-film solar cells. *ACS Energy Lett.* **2018**, *3*, 496−500.
(37) Shibuya, T.; Goto, Y.; Kamihara, Y.; Matoba, M.; Yasuoka, K.; Burton, L. A.; Walsh, A. From kesterite to stannite photovoltaics: Stability and band gaps of the $Cu_2(Zn, Fe)SnS_4$ alloy. *Appl. Phys. Lett.* **2014**, *104*, 021912.
(38) Burton, L. A.; Kumagai, Y.; Walsh, A.; Oba, F. DFT investigation into the underperformance of sulfide materials in photovoltaic applications. *J. Mater. Chem. A* **2017**, *5*, 9132−9140.
(39) Badkoobehhezaveh, A.; Abdizadeh, H.; Golobostanfard, M. Electrophoretic behavior of solvothermal synthesized anion replaced $Cu_2ZnSn(S_xSe_{1-x})_4$ films for photoelectrochemical water splitting. *Int. J. Hydrogen Energy* **2018**, *43*, 11990−12001.
(40) Ravi, V.; Scheidt, R.; DuBose, J.; Kamat, P. Hierarchical arrays of cesium lead halide perovskite nanocrystals through electrophoretic deposition. *J. Am. Chem. Soc.* **2018**, *140*, 8887−8894.
(41) Tsai, H.; Chen, C.; Thomas, S.; Hsu, C.; Tsai, W.; Chen, Y.; Wang, Y.; Wang, Z.; Hong, H.; Chueh, Y. Facile growth of Cu_2ZnSnS_4 thin-film by one-step pulsed hybrid electrophoretic and electroplating deposition. *Sci. Rep.* **2016**, *6*, 19102.
(42) Pawar, S.M.; Pawar, B.S.; Moholkar, A.V.; Choi, D.S.; Yun, J.H.; Moon, J.H.; Kolekar, S.S.; Kim, J.H. Single step electrosynthesis of Cu_2ZnSnS_4 (CZTS) thin films for solar cell application. *Electrochim. Acta* **2010**, *55*, 4057−4061.
(43) Pawar, B. S.; Pawar, S. M.; Gurav, K. V.; Shin, S. W.; Lee, J. Y.; Kolekar, S. S.; Kim, J. H. Effect of annealing atmosphere on the properties of electrochemically deposited Cu_2ZnSnS_4 (CZTS) thin films. *ISRN Renewable Energy* **2011**, *2011*, 1−5.
(44) Pawar, S.; Pawar, B.; Gurav, K.; Bae, D.; Kwon, S.; Kolekar, S.; Kim, J. Fabrication of Cu_2ZnSnS_4 thin film solar cell using single step electrodeposition method. *Jpn. J. Appl. Phys.* **2012**, *51*, 10NC27.
(45) Lee, S.; Kim, J.; Woo, H.; Jo, Y.; Huyn, J.; Inamdar, A.; Pawar, S.; Kim, H.; Jung, W.; Im, H. Structural, morphological, compositional, and optical properties of single step electrodeposited

https://dx.doi.org/10.1021/acsaem.9b02314
ACS Appl. Energy Mater. 2020, 3, 5153−5162

Cu_2ZnSnS_4 (CZTS) thin films for solar cell application. *Curr. Appl. Phys.* **2014**, *14*, 254−258.
(46) Ananthoju, B.; Sonia, F.; Kushwaha, A.; Bahadur, D.; Medhekar, N.; Aslam, M. Improved structural and optical properties of Cu_2ZnSnS_4 thin films via optimized potential in single bath electrodeposition. *Electrochim. Acta* **2014**, *137*, 154−163.
(47) Pundsack, T. J.; Chernomordik, B. D.; Beland, A. E.; Aydil, E. S.; Blank, D. A. Excited-state dynamics in CZTS nanocrystals. *J. Phys. Chem. Lett.* **2013**, *4*, 2711−2714.
(48) Opoku, F.; Govender, K. K.; van Sittert, C. G. C. E.; Govender, P. P. Recent progress in the development of semiconductor-based photocatalyst materials for applications in photocatalytic water splitting and degradation of pollutants. *Adv. Sustainable Syst.* **2017**, *1*, 1700006.

https://dx.doi.org/10.1021/acsaem.9b02314
ACS Appl. Energy Mater. 2020, 3, 5153−5162